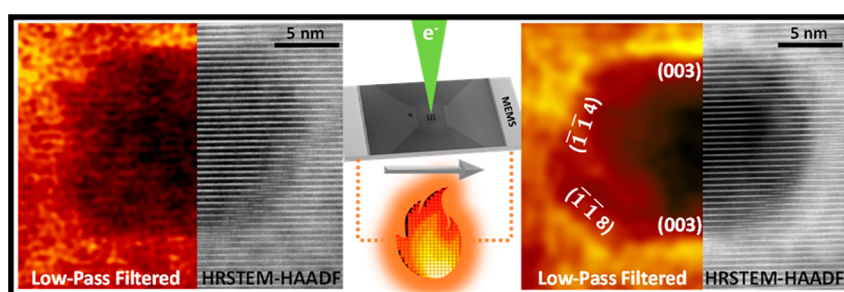# *In Situ* Monitoring of Thermally Induced Effects in Nickel-Rich Layered Oxide Cathode Materials at the Atomic Level

Anuj Pokle,* Shamail Ahmed, Simon Schweidler, Matteo Bianchini, Torsten Brezesinski, Andreas Beyer, Jürgen Janek, and Kerstin Volz*

ABSTRACT: The thermal stability of cathode active materials (CAMs) is of major importance for the safety of lithium ion batteries (LIBs). A thorough understanding of how commercially viable layered oxide CAMs behave at the atomic length scale upon heating is indispensable for the further development of LIBs. Here, structural changes of $Li(Ni_{0.85}Co_{0.15}Mn_{0.05})O_2$ (NCM851005) at elevated temperatures are studied by *in situ* aberration corrected scanning transmission electron microscopy (AC STEM). Heating NCM851005 inside the microscope under vacuum conditions enables us to observe phase transitions and other structural changes at high spatial resolutions. This has been primarily possible by establishing low dose electron beam conditions in STEM. Specific focus is put on the evolution of inherent nanopore defects found in the primary grains, which are believed to play an important role in LIB degradation. The onset temperature of structural changes is found to be ~175 °C, resulting in phase transformation from a layered to a rock salt like structure, especially at the internal interfaces, and increasing intragrain inhomogeneity. The reducing environment and heat application lead to the formation and subsequent densification of {003} and {014} type facets. In the light of these results, postsynthesis electrode drying processes applied under reducing environment and heat, for example, in the preparation of solid state batteries, should be re examined carefully.

■ INTRODUCTION

The increasing demand for improved energy density, safety, and longer cycle life is pushing the lithium ion battery (LIB) technology.[1,2] Layered lithium metal oxide cathode active materials (CAMs), especially Ni rich $Li_{1+x}(Ni_{1-y-z}Co_yMn_z)_{1-x}O_2$ (NCM), are already commercially available and applied in LIBs. Although increasing the Ni content in a CAM boosts the overall specific capacity, it results in structural instability, capacity fading, and safety issues due to outgassing.[3−11] However, the microscopic mechanisms of electrochemical and thermal degradation in Ni rich NCM are not fully understood yet. In addition, more research is required on the effect of electrode preparation methods before the cell assembly.[12−15] The drying process of electrodes, especially in the fabrication of solid state batteries (SSBs), is typically undertaken in vacuum (~100 Pa) and at high temperature conditions.[13,15,16] Because of the reducing environment and heat application (≤300 °C), the Ni rich NCM CAM can undergo structural changes even before electrochemical cycling. Furthermore, the results also shed light on CAM degradation above 300 °C that can occur in the case of a thermal runaway.[17,18] Consequently, understanding the mechanism of degradation at high temperatures in real time (*in situ*) might open up new ways to improve the material's stability. Other than temperature, the oxygen activity in the surrounding gas environment is a thermodynamic variable that influences degradation. We will, therefore, consider its effect in the Results and Discussion section.

Scanning transmission electron microscopy (STEM) is a unique characterization tool that gives structural insights at high spatial resolutions. The image contrast in the high angle annular dark field (HAADF) regime is proportional to the atomic number ($\sim Z^{1.7}$),[19,20] which helps to provide elemental information. For example, in the presence of a transition region comprising a rock salt like structure, the lithium sites will start to show intensity in the HAADF regime due to an increase in average Z, resulting from transition metal migration to these sites (after the phase transition). Likewise, thicker regions (of the same average Z) scatter more electrons, thereby providing information about changes in specimen thickness via the so called mass thickness contrast. These contrast change interpretations are crucial, specifically to track phase transitions at atomic resolution and variations in mass thickness. A substantial amount of research has been carried out on layered CAMs [e.g., NCM, $LiNi_{1-x-z}Co_xAl_zO_2$ (NCA), or $LiCoO_2$ (LCO)] to study phase transitions, crack formation, and oxygen evolution during high temperature measurements. The recent findings suggest the transformation of the layered structure and formation of a rock salt like layer at the primary grain boundaries, intragranular cracks, and additional pores formation (due to O_2 and CO_2 release) at temperatures above 200 °C.[3,4,8,21−27]

The majority of the *in situ* (heating) S/TEM work is either performed on powder samples or CAMs cycled to high voltages (4.8 V charge cutoff vs Li^+/Li).[23,28] In the present study, we concentrate on inherent defects in commercially relevant Ni rich NCM, namely, nanopores. Nanopores are already present after synthesis and have recently been shown to undergo complex structural development upon cycling.[29] We suggest that nanopores and grain boundaries play an important role in CAM degradation, in addition to the well documented role of the surface. One important aspect is to observe their thermal stability at high spatial resolution, which has yet not been reported. Additionally, structural degradation of CAM upon heating is more severe after the material underwent electrochemical cycling. In this report, we use NCM851005 (85% Ni) CAM recovered after 100 cycles (with a practical cutoff voltage of 4.2 V in a full cell with a graphite anode) to capture the effects of thermal treatment in the electrochemically cycled material.[30,31]

We investigate structural and compositional changes around nanopores in primary grains at high resolution (HR) by aberration corrected STEM (AC STEM). The sample is studied *in situ* under low dose imaging conditions employing a heating micro electromechanical system (MEMS) chip [also refer to Figure S1 in the Supporting Information (SI)] from room temperature (RT) to ~500 °C at regular temperature intervals. To ensure that the results represent a true picture of the structural development of primary grains upon heating, NCM851005 secondary particles (composed of densely packed primary grains) are used.

■ RESULTS AND DISCUSSION

Development of Internal Defects and Facet Formation. Figure 1 shows the step by step nanopore evolution at different temperatures. The nanopore is found within a primary grain in a cycled secondary particle, as shown in Figure S2 in the SI. Compared to the pore boundary at RT in Figure 1a, 1b shows a subtle change (at ~175 °C), as the contrast increases at the nanopore boundary, followed by a lower intensity at the nanopore center (also refer to Figure S3.1a,b in
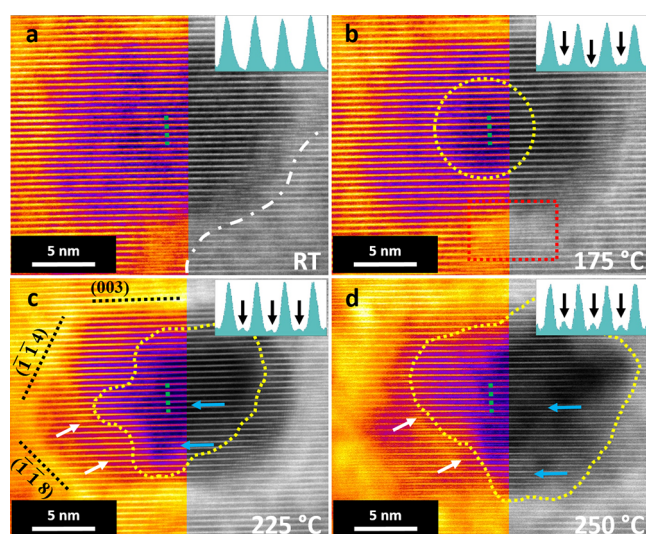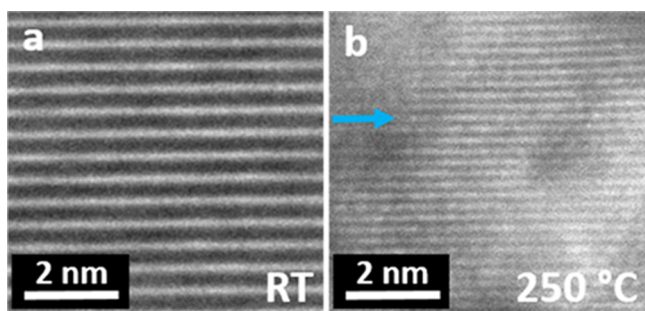

Figure 1. HAADF micrographs of the nanopore (also refer to Figure S2 in the SI) at different temperatures in the [210] zone axis with a color overlay. (a) Room temperature (RT), also showing an antiphase boundary (white line). (b) Formation of higher and lower contrast regions (red and yellow marked areas, respectively) at ~175 °C. The lower contrast region advances further in (c, d). (c) At ~225 °C, sharp boundaries and facets are formed, as denoted by the black dotted lines (also refer to Figure S3.1,3.2 in the SI). The white arrows indicate an increase in mass thickness contrast [also in (d)], and the blue arrows indicate a phase transition region, which then advances to the central region in (d) at ~250 °C. The insets show intensity profiles from the areas marked by the green dotted line in each image. The intensity peaks in (a) reflect the transition metal column intensity. The black arrows indicate the gradual appearance of intensity at the Li sites in (b−d). Also refer to Video A1 in the SI for better visualization.

the SI). This is likely due to oxygen release, which typically results in the phase transition to a rock salt like structure on the surface of Ni rich NCM CAMs.[21] The appearance of intensity peaks at the Li sites, marked by the black arrows in Figure 1b, further supports the presence of the transition region. As evident from Figure 1c,d, the peak intensity increases with increasing temperature, indicating an increasing amount of the transformed phase. At ~200 °C, the growth of other nanopores is also seen (also refer to Figure S3.1c,d in the SI). Sharp facets can be observed at ~225 °C, as shown in Figure 1c (also refer to Figure S3.2 in the SI). This suggests a correlation of the facets emerging with the occurrence of structural reconstruction layers. Transition metal (TM) migration into the interslab layer, thereby replacing Li, is observed (marked by the blue arrows in Figure 1c,d), due to the high atomic column contrast (also refer to Figure 3, marked by blue arrows). The peak intensities are displayed as insets for better tracking of phase transformation, as the TM migration is hard to visualize considering the low beam dose (refer to Video A1 for better visualization).

At elevated temperatures, we detect the onset of densification and roughness in the layered [003] direction (marked by the top dotted line in Figure 1c), followed by the appearance of sharp (1 1 4) and (1 1 8) plane facets (also refer to Figure S3.2 in the SI). This shows that the formation of the reconstruction layer is not uniform and highly dependent on the crystalline facets. A similar observation was made on $LiNi_{0.80}Co_{0.15}Al_{0.05}O_2$ primary nanoparticles by

Zhang et al., where a rough reconstruction morphology appears at the (003) surfaces compared to the non (003) type facets.[32] Interestingly, it was predicted that the growth of relatively sharp non (003) type facets becomes favorable in a reducing environment (due to the high vacuum condition in S/TEM) and during heating.[33] To the best of our knowledge, this theoretical prediction has never been proven experimentally before. As the temperature is increased further to ~250 °C, the nanopore boundary gets diffuse, displaying high mass thickness contrast (white arrows) along with phase transition regions (blue arrows in Figure 1d). Nonetheless, similar to electrochemical cycling, sharp boundary and facet formation (from ~175 to ~225 °C, Figure 1b,c), followed by diffuse boundaries (at ~250 °C, Figure 1d), are observed.[29]

One can clearly observe the layered to rock salt like transition because of TM migration at the nanopore boundary area as the dominant process, which can be seen in more detail in Figure 2. Here, a comparison of a nanopore boundary at RT

Figure 2. HAADF micrograph in the [210] zone axis of the same nanopore boundary region (also refer to Figure S4 in the SI) showing (a) layered structure at room temperature (RT) and (b) transition into a rock salt like structure at ~250 °C.

and after heating to ~250 °C is shown. The HR STEM micrograph was obtained from the region illustrated in Figure S4 in the SI. The comparison of Figure 2a,b clearly shows that the nanopore boundary encounters a phase transition from a layered to the rock salt like structure. It is important to note that the image in Figure 2b was obtained by focussing the STEM probe on the boundary area, as compared to Figure 1d. The focus plane from the nanopore central region to the boundary area significantly changes (also refer to Figure S4b in the SI). This is not the case for the RT image in Figure S4a in the SI, thus highlighting the fact that the rock salt like reconstructed phase grows epitaxially on the layered phase.

These observations are similar to previous results from *ex situ* experiments on electrochemically cycled NCM851005 (driven by oxygen release and surface reconstruction).[29] This suggests that prolonged electrochemical cycling and application of heat may have a similar effect on nanopore evolution. Oxygen release is inevitably linked with structural rearrangement, which has been shown to occur during the initial electrochemical cycles, depending on the charge cutoff potential (or state of charge).[34−36] We will discuss the apparently similar effect of electrochemical cycling and application of heat in some more detail in the final section.

Thermal Stability of the Antiphase Boundary (APB). Defects, including APBs, are believed to cause hindrance to lithium pathways within otherwise homogeneous materials, and their effects on the performance of CAMs are much under debate.[37,38] In the case of oxide CAMs, to the best of our

knowledge, APBs have only been observed in epitaxially grown LCO thin films and electrochemically cycled spinel $LiNi_{0.5}Mn_{1.5}O_4$ (LNMO).[39−42] It should be noted that we refer to APBs for simplicity here, but what is found in ionic crystals would be more appropriately described as cationic APBs, i.e., the antiphase defect affects the cationic sublattice while leaving the oxygen one unaffected.[43] At the nanopore edge within a primary grain, we found an APB, which is denoted as a white line in Figure 1a. Because we are using a sample that has been electrochemically cycled, we suggest the APB may have formed as a consequence of inhomogeneous Li ion transport, especially during the delithiation process.[41,44] Nevertheless, the APB formation may as well have been a result of the material's synthesis process.[45] Because the role of nanopores in the formation of APBs in Ni rich NCM has not been clarified yet, it clearly needs further study.

Figure 3 shows an in depth analysis of the stability of such APB at elevated temperatures. Even though the nanopore underwent phase transformation on its surface with new facet formation (also refer to Figure S3.2 in the SI), the APB region is found to be stable up to ~275 °C, after which imaging is not
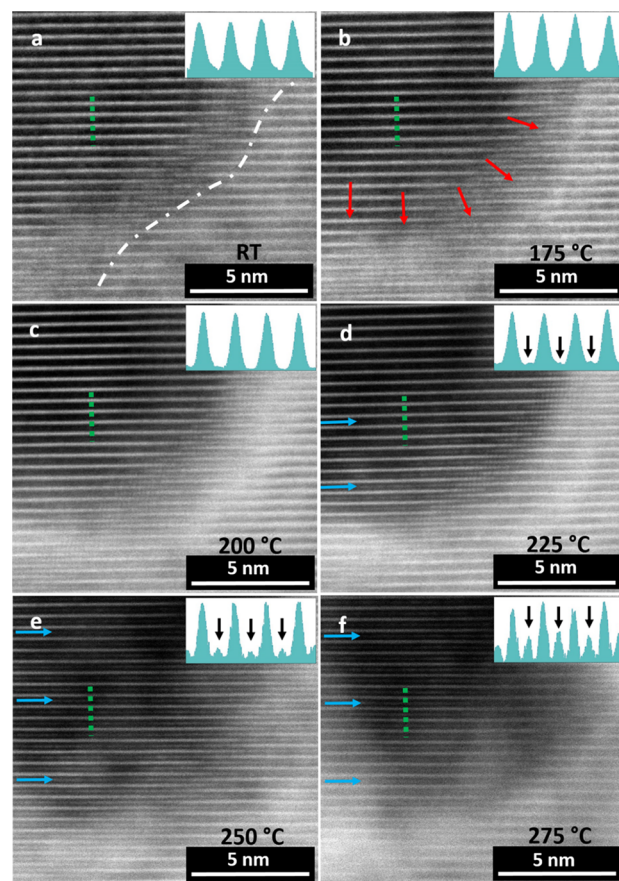
Figure 3. HAADF micrographs showing the antiphase boundary (marked by the white line) at different temperatures. (a) At room temperature (RT), (b) ~175 °C, (c) ~200 °C, (d) ~225 °C, (e) ~250 °C, and (f) ~275 °C. The red arrows in (b) denote the brighter rim formation, whereas the blue arrows in (d−f) indicate the phase transition region within the nanopore area. The insets are intensity profiles from the area denoted by the green dotted lines. The four peaks in (a−c) reflect the transition metal column intensity. (d−f) Gradual appearance of intensity at the Li sites is indicated by black arrows.

possible due to rapid structural disorder and specimen drift. The inhomogeneity in TM distribution at high temperatures can be seen when comparing the boundaries of the nanopore defect area. The intensity at the Li sites, which provides clear evidence of TM migration, previously emerged at ~175 °C (Figure 1b). Interestingly, this is observed near the APB only at ~225 °C (Figure 3d), suggesting that the phase transition close to the APB occurs at higher temperatures. In addition, no evidence of new facet formation is found in the APB area, as compared to the rest of the nanopore boundary region. The observations of a higher onset temperature for decomposition and absence of new facets indicate better stability of nanopore regions in the presence of APBs, which may then be exploited as a useful tool in tailoring the structural integrity and therefore the electrochemical properties of CAMs.[39,46,47]

Nanoparticle-like Growth in the TM-Enriched Regions. The thermal stability of the CAM plays a crucial role in triggering thermal runaway situations, where temperatures well above 250 °C can be reached (more details in the final section).[18] Hence, here, we study the NCM evolution and, in particular, the nanopore regions at these elevated temperatures. At temperatures > 250 °C, the stage drift is significant and collecting data at high spatial resolutions is challenging. The bending of the silicon carbide/nitride membrane (MEMS chip) at elevated temperatures adds to the challenge. Acceleration in structural modulations across the primary grains at high temperatures is also seen. An increase in mass thickness contrast is noticeable at ~275 °C in Figure 4a (also
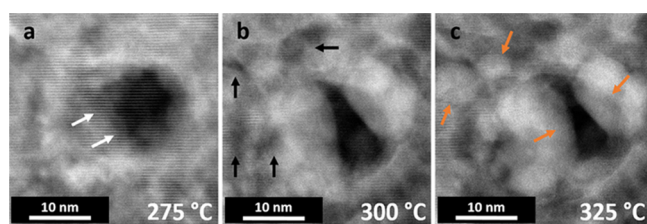
Figure 4. HAADF micrographs (a) at ~275 °C showing an increase in mass thickness contrast (white arrows), (b) at ~300 °C showing TM depleted regions (black arrows), and (c) at ~325 °C showing apparent nanoparticle like growth at the nanopore boundary and its vicinity (orange arrows). Also, refer to Video A2 in the SI.

refer to Videos A1 and A2 in the SI). Figure 4b,c shows the transition of the nanopore edges into a nanoparticle like phase from ~275 to ~325 °C, as denoted by orange arrows in Figure 4c. The appearance of TM depleted regions (denoted by black arrows in Figure 4b), followed by TM enriched regions (denoted by orange arrows in Figure 4c), indicates the formation of a TM rich nanoparticle like microstructure of amorphous nature. Nanoparticle like growth was found to be dynamic and unstable. Furthermore, a rapid change in mass thickness contrast, particularly in the layered direction, is observed at ~400 °C (Figure 5). Investigating the primary grains at HR revealed a polycrystalline rock salt type phase (also refer to Figure S5 in the SI). The polycrystalline nature of the primary grain makes orientation in a specific zone axis challenging.

To further drive the transformation process, the temperature was increased to ~500 °C, placing the NCM in an even more reducing environment. At this temperature, separation into two phases were observed. A nanoparticle phase is confirmed, which was e beam robust, next to extremely e beam sensitive
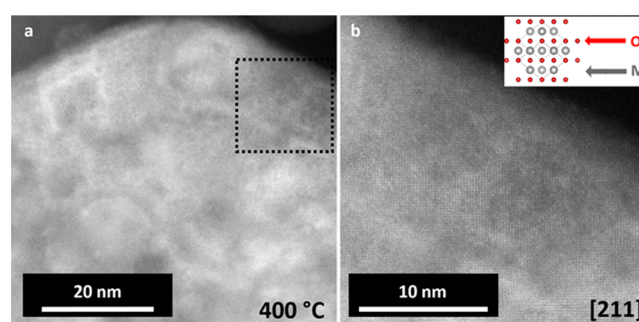

Figure 5. (a) HAADF micrographs of a primary grain at ~400 °C. (b) Zoomed in region marked in (a) showing rock salt like nature. The inset in (b) is the respective rock salt model in the [211] zone axis with oxygen atoms in red and transition metals in gray (also refer to Figure S5 in the SI).

degraded regions (also refer to Figure S6 in the SI). Interestingly, Hwang et al. reported the formation of pure Ni nanoparticles on the surface of the cathode at elevated temperatures of ~400 °C.[3] However, the sample was prepared by sonicating powdered material to ensure proper dispersion of nanoparticles. Because the CAM under investigation here is in the form of a secondary particle, the grain boundary potential may play a role in the degradation process.[48] As can be seen in Figure S7a in the SI, the HR micrograph of Ni nanoparticles has a face centered cubic [110] structural appearance. Even though the Ni nanoparticles were e beam robust, HR imaging is not trivial. Structural modulation is induced while scanning, as Ni exhibits ferromagnetic behavior,[49] and the presence of the objective lens magnetic field inside the S/TEM column is also problematic (~2−3 T).[50]

To gain further chemical information, energy dispersive X ray (EDX) spectroscopy and electron energy loss spectroscopy (EELS) were performed. Figure 6a shows the EDX map of Ni obtained from the region marked in Figure S6 in the SI. Because the EDX spectra in the degraded region were not conclusive due to damage, EELS data of the Li K edge, the O K edge, and the Ni L edge were collected.[51−53] Apart from the presence of the Ni L edge (Figure 6b, red line), the absence of the O K edge (Figure 6c, red line) confirms the presence of reduced, likely Ni metal nanoparticles. On the contrary, the degraded area showed the presence of oxygen (Figure 6c, blue line) with a subtle Ni L edge signal (Figure 6b, blue line). The absence of an O K pre edge (below 530 eV) in the degraded regions further confirms complete transformation (decom position) of the layered structure. Nonetheless, interpreting EELS data taken from e beam sensitive regions is challenging.

The presence of Ni in the degraded region is also supported by capturing the dynamics of the atomic clusters (also refer to Video A3 in the SI). Additionally, the Ni M edge is present in both phases, with a subtle Li K edge signal in the degraded area, as shown in the inset of Figure S6 in the SI. This confirms that the degraded area mostly contains lithia (Li_2O),[52] decorated by Ni atomic clusters in a rock salt like NiO phase. To further confirm the proposed phases of Ni, NiO, and Li_2O, precession electron diffraction (PED) was performed on the same nanoparticle region.[54,55] Coupled with the ASTAR tool, the scanned precession patterns showed the nanoparticle to be composed of Ni metal surrounded by "NiO" and Li_2O phases (refer to Figure S7b,c in the SI). Hence, investigating the CAM *in situ* at various steps from RT to ~500 °C reveals a complex deterioration mechanism
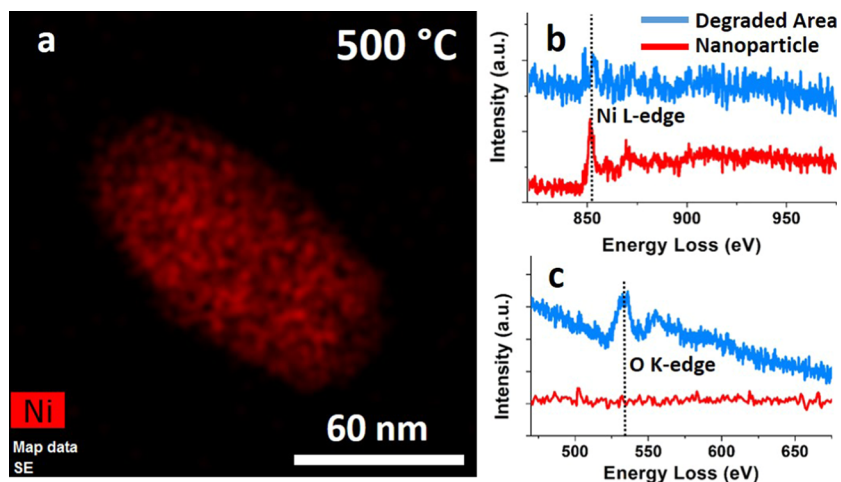
Figure 6. (a) EDX map of Ni at ~500 °C. EEL spectra of (b) Ni L edge (~852 eV) and (c) O K edge (~530 eV). The spectra in blue were collected from the degraded area, and those in red were collected from the nanoparticle. Also refer to Figures S6 and S7 in the SI for further EDX, HR STEM, and PED analyses.

$$Li_x(NCM)O_2 \rightarrow Li_2O + Li_\delta Ni_{1-\delta}O + Ni_{NANO} + O_2$$
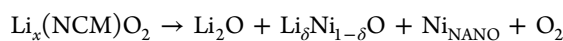
where the stoichiometric coefficients are omitted.

The overall results suggest a structural transformation from a layered to a rock salt like structure, accompanied by TM reduction, which agrees well with the thermal decomposition studies done using X ray diffraction (XRD). Even the formation of a metallic phase (most probably Ni) has been reported in some cases under rather reducing conditions.[21,24,56] However, we note that the cause of this was most likely due to the fact that the experiment was conducted under an inert atmosphere (using He as a carrier gas for mass spectrometry) rather than heating in air or oxygen. As STEM enables us to gain structural and chemical information at high spatial resolutions, we can conclude that the pore and grain boundaries act as catalyzing sites for nanoparticle formation. This suggests that along with the grain boundaries, the nanopore boundaries also play a role in the thermal degradation process.

Comparison of Structural Changes to Cycling and Its Implications. Finally, we compare the structural changes observed during the *in situ* heating experiment to those of long term cycled NCM851005, investigated in our previous *ex situ* study. There, a pristine sample was compared to samples that were electrochemically cycled 200 and 500 times. The latter ones revealed structural changes from the layered to the rock salt like phase in and around the nanopores.[29] The *in situ* heating experiment shows a similar structural reconstruction around the nanopore in real time and the densification of facets. The facet appearance at ~225 °C (Figure 1) is comparable to that of the sample after 200 cycles (also refer to Figure S8 in the SI). The ultrahigh vacuum in the S/TEM column ($p \approx 1.2 \times 10^{-5}$ Pa) changes the oxygen chemical potential, which thermodynamically destabilizes the NCM CAM and significantly facilitates the loss of oxygen. In a LIB, some oxygen is instead lost at a high state of charge, resulting in the analogous formation of a rock salt type surface. The application of heat enhances the transformation into the rock salt like phase at the nanopore boundaries, followed by Ni nanoparticle formation.[27] In case of the electrochemically cycled samples, the structural degradation process takes much

longer due to slower kinetics at lower temperatures (it typically occurs during the course of prolonged cycling).

One should note that our findings are also relevant to SSB cell preparation, where common practice is to dry the electrode in vacuum at elevated temperatures (up to ~300 °C) for a certain time (up to ~12 h).[15,57] In our *in situ* STEM experiments, at such conditions, the primary grains undergo major phase transitions already, prior to any electrochemical characterization. This might also be the reason for the findings of Pritzl et al.,[13] where it is reported that the battery capacity is substantially reduced when the drying temperature of NCM851005 (after a washing process) is increased from 25 to 300 °C. Further work is required in the future to verify the applicability of our findings to real battery working conditions. Meanwhile, our work serves as an important note of caution for experimentalists processing CAMs and using high temper atures in doing so, both for liquid and solid state battery applications.

Furthermore, our study on the heating of CAMs above 300 °C is relevant to unforeseen battery failure situations. If the temperature in LIB exceeds a critical level, a chain reaction can lead to thermal runaway. In this case, temperatures can increase exponentially, reaching values even beyond 800 °C.[17,18] Hence, the present study enables us to understand the CAM degradation mechanism, even in critical failure situations.

■ CONCLUSIONS

In this report, we carried out an *in situ* thermal investigation of nanopore development in NCM851005 CAM using STEM. We have observed that structural changes occur at ~175 °C and a further temperature increase results in the densification of the nanopore boundaries, which form facets at ~225 °C. At higher temperatures, the newly formed sharp facets get diffuse, showing a rock salt like phase. We found that the primary grain response upon heating at moderate temperatures is similar to what is observed regarding the phase change during prolonged electrochemical cycling. At higher temperatures, Ni nano particle formation is apparent, which is not the case in battery cycling. Intriguingly, under heat application, the theoretical prediction of the development of rough (003) and sharper non (003) type facets was seen experimentally for the first

time. The thermal stability of an APB region was proven at high spatial resolution (up to ~275 °C), which seems to preserve the structural integrity around the nanopore.

Further heating of the primary grains reveals an elaborate phase transition from the layered to the rock salt like structure, followed by nanoparticle formation. The nanoparticle like structure formation in TM rich regions unfolds the role of nanopores in the degradation mechanism. In the final stage of thermal decomposition at ~500 °C, separation of NCM primary grains into metal nanoparticles (Ni) and Li_2O decorated by Ni clusters occur. Importantly, the results in the low to medium temperature range also suggest reconsidering cell preparation guidelines (i.e., the electrode/CAM drying processes) for both LIBs and SSBs.

■ EXPERIMENTAL DETAILS

Synthesis of NCM851005, Cell Construction, and Electrochemical Characterization. The samples were prepared as described in ref [29]. Since the sample cycled to 200 cycles and above showed severe local phase transformations like nanopore boundary evolution (with facet formation) and formation of polycrystallinity with oxygen channels within the primary grains,[29] a lower cycled (100 cycles) sample was chosen to observe the thermal impact in an electrochemically cycled CAM. Only Figure S8 in the SI is obtained from a sample cycled to 200 cycles to compare the structure modulation with the sample under heat treatment.

Sample Preparation. SEM imaging and S/TEM sample preparation were done using a JEOL JIB 4601F dual beam system capable of operating at 1−30 kV for the electron and Ga ion beam, respectively. The secondary particle of an NCM851005 electrode, which was cycled for 100 times, was first coated using an e beam assisted carbon and tungsten (C/W) deposition, followed by a Ga ion assisted 2 μm thick C/W layer. The secondary particle was then lifted using a micromanipulator and attached to a TEM omniprobe Cu grid having a preprepared Si lamella, as shown in Figure S1b in the SI. This was done to avoid W redeposition on the NCM lamella in the second transfer step.

A cross sectional, electron transparent sample is achieved by thinning using 30, 15, 10, and 5 kV, followed by a 3 kV ion beam. For final polishing, a Fischione NanoMill 1040 is used to perform gentle milling using an Ar ion beam. The lamella is then transferred to the heating MEMS chip. Refer to Figure S1 in the SI for further illustrations.

Material Characterization. A double Cs corrected JEOL JEM 2200 FS equipped with an in column omega filter was exploited for STEM characterization. All images in this paper are high angle annular dark field (HAADF) images taken by setting the inner and outer angles of the annular dark field detector to 70 and 180 mrad, respectively. The microscope was operated at 200 kV with a 15.07 mrad convergence angle. The beam current used was ~6 pA. Image analysis (including intensity profiles) was carried out using Gatan Digital Micrograph and ImageJ software. The structure models in the inset were obtained from VESTA software.[58] The influence of the beam damage was reduced by collecting several individual fast acquisitions and aligning by the Smart Align script.[59] During HR STEM acquisition, the e beam dose was restricted to ~5000 eÅ^{-2}, and for higher temperatures of ~275 °C, the dose was further reduced to ~2500 eÅ^{-2}. Here, it is important to note that the electron dose used in previous studies while acquiring HR images was significantly higher at ~10^6 eÅ^{-2}.[23] High e beam dose will primarily result in e beam induced changes, followed by damaging the structure if one plans to collect sequential data at different temperatures at the same region.[51,60] The Ni, NiO, and Li_2O phase maps were obtained with a JEOL JEM 3010 300 kV LaB_6 cathode filament equipped with an ASTAR (NanoMEGAS) device. The PED patterns were obtained with the lowest e beam dose possible using the smallest condenser aperture at spot size 5. The crystallographic information framework (CIF) files of Ni metal, NiO, and Li_2O were received from the Inorganic Crystal Structure Database (ICSD) to generate the diffraction templates. The spatial resolution and phase identification reliability are limited by the electron gun type, spherical aberration (Cs), beam diameter (~10 nm), and the precession angle (~0.6°).

Although the electron dose was kept at a minimum, it is crucial to verify the role of e beam induced effects. An overview image is shown in Figure S9 in the SI taken before and after heating to ~400 °C. The nanoparticle like formation was seen throughout the primary grains, especially at the grain boundaries (with bright rim like formations marked with orange arrows). It is important to note that the regions that did not see any e beam during heating also showed the nanoparticle like phase appearance. This excludes a mere e beam induced effect. However, one cannot completely ignore the influence of the beam, as we did observe more nanoparticle like formation in the investigated primary grain (black dotted rectangle in Figure S9 in the SI). Nonetheless, the onset of nanoparticle like formations in the TM enriched regions at the nanopore/grain boundaries was observed throughout the secondary particle.

The *in situ* STEM heating experiment was performed on the Protochip Fusion holder using a MEMS chip having SiN windows. The sample was prepared by a focused ion beam (FIB) preparation approach to mimic the real grain boundary conditions, unlike in the case of standalone nanoparticles.[3,4,8] The MEMS chip was used, as it has precise heating control. Also, refer to Figure S1 in the SI. The temperature was increased at a rate of 0.1 °C/s, and data were collected after every 15 °C increase (holding for 5 min each before collecting any data). By FIB, the center SiN window was removed before placing the lamella. This ensured better spatial resolution with a lower beam dose.

■ AUTHOR INFORMATION

Corresponding Authors
Anuj Pokle − *Materials Science Center (WZMW) and Department of Physics, Philipps University Marburg, 35032 Marburg, Germany;* ⊙ orcid.org/0000 0002 7457 8839; Email: pokle@staff.uni marburg.de

Kerstin Volz − *Materials Science Center (WZMW) and Department of Physics, Philipps University Marburg, 35032 Marburg, Germany;* Email: volz@staff.uni marburg.de

Authors
Shamail Ahmed − *Materials Science Center (WZMW) and Department of Physics, Philipps University Marburg, 35032 Marburg, Germany*

Simon Schweidler − *Battery and Electrochemistry Laboratory, Institute of Nanotechnology, Karlsruhe Institute of Technology (KIT), 76344 Eggenstein Leopoldshafen, Germany;* ⊙ orcid.org/0000 0003 4675 1072

Matteo Bianchini − *Battery and Electrochemistry Laboratory, Institute of Nanotechnology, Karlsruhe Institute of Technology (KIT), 76344 Eggenstein Leopoldshafen, Germany; BASF SE, 67056 Ludwigshafen, Germany*

Torsten Brezesinski − *Battery and Electrochemistry Laboratory, Institute of Nanotechnology, Karlsruhe Institute of Technology (KIT), 76344 Eggenstein Leopoldshafen, Germany;* ⦿ orcid.org/0000 0002 4336 263X

Andreas Beyer − *Materials Science Center (WZMW) and Department of Physics, Philipps University Marburg, 35032 Marburg, Germany;* ⦿ orcid.org/0000 0001 6533 0631

Jürgen Janek − *Battery and Electrochemistry Laboratory, Institute of Nanotechnology, Karlsruhe Institute of Technology (KIT), 76344 Eggenstein Leopoldshafen, Germany; Institute of Physical Chemistry & Center for Materials Research, Justus Liebig University, 35392 Giessen, Germany;* ⦿ orcid.org/0000 0002 9221 4756

Notes

The authors declare no competing financial interest.

■ REFERENCES

(1) Whittingham, M. S. Lithium Batteries and Cathode Materials. *Chem. Rev.* **2004**, *104*, 4271−4302.

(2) Zhang, Y.; Zuo, T. T.; Popovic, J.; Lim, K.; Yin, Y. X.; Maier, J.; Guo, Y. G. Towards Better Li Metal Anodes: Challenges and Strategies. *Mater. Today* **2020**, *33*, 56−74.

(3) Hwang, S.; Kim, S. M.; Bak, S. M.; Cho, B. W.; Chung, K. Y.; Lee, J. Y.; Chang, W.; Stach, E. A. Investigating Local Degradation and Thermal Stability of Charged Nickel Based Cathode Materials through Real Time Electron Microscopy. *ACS Appl. Mater. Interfaces* **2014**, *6*, 15140−15147.

(4) Hwang, S.; Kim, S. M.; Bak, S. M.; Kim, S. Y.; Cho, B. W.; Chung, K. Y.; Lee, J. Y.; Stach, E. A.; Chang, W. Using Real Time Electron Microscopy To Explore the Effects of Transition Metal Composition on the Local Thermal Stability in Charged $Li_xNi_yMn_zCo_{1−y−z}O_2$ Cathode Materials. *Chem. Mater.* **2015**, *27*, 3927−3935.

(5) Bianchini, M.; Roca Ayats, M.; Hartmann, P.; Brezesinski, T.; Janek, J. There and Back Again—The Journey of $LiNiO_2$ as a Cathode Active Material. *Angew. Chem., Int. Ed.* **2019**, *58*, 10434−10458.

(6) Chen, Z.; Ren, Y.; Lee, E.; Johnson, C.; Qin, Y.; Amine, K. Study of Thermal Decomposition of $Li_{1−x}(Ni_{1/3}Mn_{1/3}Co_{1/3})_{0.9}O_2$ Using In Situ High Energy X Ray Diffraction. *Adv. Energy Mater.* **2013**, *3*, 729−736.

(7) Ma, S.; Jiang, M.; Tao, P.; Song, C.; Wu, J.; Wang, J.; Deng, T.; Shang, W. Temperature Effect and Thermal Impact in Lithium Ion Batteries: A Review. *Prog. Nat. Sci.: Mater. Int.* **2018**, *28*, 653−666.

(8) Mu, L.; Lin, R.; Xu, R.; Han, L.; Xia, S.; Sokaras, D.; Steiner, J. D.; Weng, T. C.; Nordlund, D.; Doeff, M. M.; Liu, Y.; Zhao, K.; Xin, H. L.; Lin, F. Oxygen Release Induced Chemomechanical Breakdown of Layered Cathode Materials. *Nano Lett.* **2018**, *18*, 3241−3249.

(9) Dahn, J. R.; Fuller, E. W.; Obrovac, M.; von Sacken, U. Thermal Stability of Li_xCoO_2, Li_xNiO_2 and $λ MnO_2$ and Consequences for the Safety of Li Ion Cells. *Solid State Ionics* **1994**, *69*, 265−270.

(10) Arai, H.; Okada, S.; Sakurai, Y.; Yamaki, J. Thermal Behavior of $Li_{1−y}NiO_2$ and the Decomposition Mechanism. *Solid State Ionics* **1998**, *109*, 295−302.

(11) Lee, K. K.; Yoon, W. S.; Kim, K. B.; Lee, K. Y.; Hong, S. T. A Study on the Thermal Behavior of Electrochemically Delithiated $Li_{1−x}NiO_2$. *J. Electrochem. Soc.* **2001**, *148*, A716−A722.

(12) Kremer, L. S.; Hoffmann, A.; Danner, T.; Hein, S.; Prifling, B.; Westhoff, D.; Dreer, C.; Latz, A.; Schmidt, V.; Wohlfahrt Mehrens, M. Manufacturing Process for Improved Ultra Thick Cathodes in High Energy Lithium Ion Batteries. *Energy Technol.* **2020**, *8*, No. 1900167.

(13) Pritzl, D.; Teufl, T.; Freiberg, A. T. S.; Strehle, B.; Sicklinger, J.; Sommer, H.; Hartmann, P.; Gasteiger, H. A. Editors' Choice— Washing of Nickel Rich Cathode Materials for Lithium Ion Batteries: Towards a Mechanistic Understanding. *J. Electrochem. Soc.* **2019**, *166*, A4056.

(14) Wu, Y.; Li, M.; Wahyudi, W.; Sheng, G.; Miao, X.; Anthopoulos, T. D.; Huang, K. W.; Li, Y.; Lai, Z. Performance and Stability Improvement of Layered NCM Lithium Ion Batteries at High Voltage by a Microporous Al_2O_3 Sol−Gel Coating. *ACS Omega* **2019**, *4*, 13972−13980.

(15) Randau, S.; Weber, D. A.; Kötz, O.; Koerver, R.; Braun, P.; Weber, A.; Ivers Tiffée, E.; Adermann, T.; Kulisch, J.; Zeier, W. G.; Richter, F. H.; Janek, J. Benchmarking the Performance of All Solid State Lithium Batteries. *Nat. Energy* **2020**, *5*, 259−270.

(16) Yudha, C. S.; Muzayanha, S. U.; Widiyandari, H.; Iskandar, F.; Sutopo, W.; Purwanto, A. Synthesis of $LiNi_{0.85}Co_{0.14}Al_{0.01}O_2$ Cathode Material and Its Performance in an NCA/Graphite Full Battery. *Energies* **2019**, *12*, 1886.

(17) Sharifi Asl, S.; Lu, J.; Amine, K.; Shahbazian Yassar, R. Oxygen Release Degradation in Li Ion Battery Cathode Materials: Mecha nisms and Mitigating Approaches. *Adv. Energy Mater.* **2019**, *9*, No. 1900551.

(18) Liu, X.; Ren, D.; Hsu, H.; Feng, X.; Xu, G. L.; Zhuang, M.; Gao, H.; Lu, L.; Han, X.; Chu, Z.; Li, J.; He, X.; Amine, K.; Ouyang, M. Thermal Runaway of Lithium Ion Batteries without Internal Short Circuit. *Joule* **2018**, *2*, 2047−2064.

(19) Nellist, P. D. The Principles of STEM Imaging. In *Scanning Transmission Electron Microscopy*; Pennycook, S. J.; Nellist, P. D., Eds.; Springer New York: New York, NY, 2011; pp 91−115.

(20) Nellist, P. D.; Pennycook, S. J. The Principles and Interpretation of Annular Dark Field Z Contrast Imaging. In *Advances in Imaging and Electron Physics*; Hawkes, P. W., Ed.; Elsevier, 2000; Vol. *113*, pp 147−203.

(21) Bak, S. M.; Hu, E.; Zhou, Y.; Yu, X.; Senanayake, S. D.; Cho, S. J.; Kim, K. B.; Chung, K. Y.; Yang, X. Q.; Nam, K. W. Structural Changes and Thermal Stability of Charged $LiNi_xMn_yCo_zO_2$ Cathode Materials Studied by Combined In Situ Time Resolved XRD and Mass Spectroscopy. *ACS Appl. Mater. Interfaces* **2014**, *6*, 22594−22601.

(22) Sharifi Asl, S.; Soto, F. A.; Nie, A.; Yuan, Y.; Asayesh Ardakani, H.; Foroozan, T.; Yurkiv, V.; Song, B.; Mashayek, F.; Klie, R. F.; Amine, K.; Lu, J.; Balbuena, P. B.; Shahbazian Yassar, R. Facet Dependent Thermal Instability in $LiCoO_2$. *Nano Lett.* **2017**, *17*, 2165−2171.

(23) Yan, P.; Zheng, J.; Chen, T.; Luo, L.; Jiang, Y.; Wang, K.; Sui, M.; Zhang, J. G.; Zhang, S.; Wang, C. Coupling of Electrochemically Triggered Thermal and Mechanical Effects to Aggravate Failure in a Layered Cathode. *Nat. Commun.* **2018**, *9*, No. 2437.

(24) Nam, K. W.; Bak, S. M.; Hu, E.; Yu, X.; Zhou, Y.; Wang, X.; Wu, L.; Zhu, Y.; Chung, K. Y.; Yang, X. Q. Combining In Situ Synchrotron X Ray Diffraction and Absorption Techniques with Transmission Electron Microscopy to Study the Origin of Thermal Instability in Overcharged Cathode Materials for Lithium Ion Batteries. *Adv. Funct. Mater.* **2013**, *23*, 1047−1063.

(25) Yuan, Y.; Amine, K.; Lu, J.; Shahbazian Yassar, R. Under standing Materials Challenges for Rechargeable Ion Batteries with in Situ Transmission Electron Microscopy. *Nat. Commun.* **2017**, *8*, No. 15806.

(26) Guilmard, M.; Croguennec, L.; Denux, D.; Delmas, C. Thermal Stability of Lithium Nickel Oxide Derivatives. Part I: $Li_xNi_{1.02}O_2$ and $Li_xNi_{0.89}Al_{0.16}O_2$ (x = 0.50 and 0.30). *Chem. Mater.* **2003**, *15*, 4476−4483.

(27) Zhang, H.; May, B. M.; Omenya, F.; Whittingham, M. S.; Cabana, J.; Zhou, G. Layered Oxide Cathodes for Li Ion Batteries:

Oxygen Loss and Vacancy Evolution. *Chem. Mater.* **2019**, *31*, 7790−7798.

(28) Yan, P.; Zheng, J.; Gu, M.; Xiao, J.; Zhang, J. G.; Wang, C. M. Intragranular Cracking as a Critical Barrier for High Voltage Usage of Layer Structured Cathode for Lithium Ion Batteries. *Nat. Commun.* **2017**, *8*, No. 14101.

(29) Ahmed, S.; Pokle, A.; Schweidler, S.; Beyer, A.; Bianchini, M.; Walther, F.; Mazilkin, A.; Hartmann, P.; Brezesinski, T.; Janek, J.; Volz, K. The Role of Intragranular Nanopores in Capacity Fade of Nickel Rich Layered Li(Ni$_{1-x-y}$Co$_x$Mn$_y$)O$_2$ Cathode Materials. *ACS Nano* **2019**, *13*, 10694−10704.

(30) Schweidler, S.; de Biasi, L.; Garcia, G.; Mazilkin, A.; Hartmann, P.; Brezesinski, T.; Janek, J. Investigation into Mechanical Degradation and Fatigue of High Ni NCM Cathode Material: A Long Term Cycling Study of Full Cells. *ACS Appl. Energy Mater.* **2019**, *2*, 7375−7384.

(31) Schweidler, S.; de Biasi, L.; Hartmann, P.; Brezesinski, T.; Janek, J. Kinetic Limitations in Cycled Nickel Rich NCM Cathodes and Their Effect on the Phase Transformation Behavior. *ACS Appl. Energy Mater.* **2020**, *3*, 2821−2827.

(32) Zhang, H.; May, B. M.; Serrano Sevillano, J.; Casas Cabanas, M.; Cabana, J.; Wang, C.; Zhou, G. Facet Dependent Rock Salt Reconstruction on the Surface of Layered Oxide Cathodes. *Chem. Mater.* **2018**, *30*, 692−699.

(33) Cho, E.; Seo, S. W.; Min, K. Theoretical Prediction of Surface Stability and Morphology of LiNiO$_2$ Cathode for Li Ion Batteries. *ACS Appl. Mater. Interfaces* **2017**, *9*, 33257−33266.

(34) Jung, R.; Metzger, M.; Maglia, F.; Stinner, C.; Gasteiger, H. A. Oxygen Release and Its Effect on the Cycling Stability of LiNi$_x$Mn$_y$Co$_z$O$_2$ (NMC) Cathode Materials for Li Ion Batteries. *J. Electrochem. Soc.* **2017**, *164*, A1361−A1377.

(35) Strehle, B.; Kleiner, K.; Jung, R.; Chesneau, F.; Mendez, M.; Gasteiger, H. A.; Piana, M. The Role of Oxygen Release from Li and Mn Rich Layered Oxides during the First Cycles Investigated by On Line Electrochemical Mass Spectrometry. *J. Electrochem. Soc.* **2017**, *164*, A400−A406.

(36) Strauss, F.; Teo, J. H.; Schiele, A.; Bartsch, T.; Hatsukade, T.; Hartmann, P.; Janek, J.; Brezesinski, T. Gas Evolution in Lithium Ion Batteries: Solid versus Liquid Electrolyte. *ACS Appl. Mater. Interfaces* **2020**, *12*, 20462−20468.

(37) Islam, M. S.; Driscoll, D. J.; Fisher, C. A. J.; Slater, P. R. Atomic Scale Investigation of Defects, Dopants, and Lithium Transport in the LiFePO$_4$ Olivine Type Battery Material. *Chem. Mater.* **2005**, *17*, 5085−5092.

(38) Eames, C.; Clark, J. M.; Rousse, G.; Tarascon, J. M.; Islam, M. S. Lithium Migration Pathways and Van Der Waals Effects in the LiFeSO$_4$OH Battery Material. *Chem. Mater.* **2014**, *26*, 3672−3678.

(39) Ong, P. V.; Yang, Z.; Sushko, P. V.; Du, Y. Formation, Structural Variety, and Impact of Antiphase Boundaries on Li Diffusion in LiCoO$_2$ Thin Film Cathodes. *J. Phys. Chem. Lett.* **2018**, *9*, 5515−5520.

(40) Tan, H.; Takeuchi, S.; Bharathi, K. K.; Takeuchi, I.; Bendersky, L. A. Microscopy Study of Structural Evolution in Epitaxial LiCoO$_2$ Positive Electrode Films during Electrochemical Cycling. *ACS Appl. Mater. Interfaces* **2016**, *8*, 6727−6735.

(41) Gong, Y.; Zhang, J.; Jiang, L.; Shi, J. A.; Zhang, Q.; Yang, Z.; Zou, D.; Wang, J.; Yu, X.; Xiao, R.; Hu, Y. S.; Gu, L.; Li, H.; Chen, L. In Situ Atomic Scale Observation of Electrochemical Delithiation Induced Structure Evolution of LiCoO$_2$ Cathode in a Working All Solid State Battery. *J. Am. Chem. Soc.* **2017**, *139*, 4274−4277.

(42) Gong, Y.; Chen, Y.; Zhang, Q.; Meng, F.; Shi, J. A.; Liu, X.; Liu, X.; Zhang, J.; Wang, H.; Wang, J.; Yu, Q.; Zhang, Z.; Xu, Q.; Xiao, R.; Hu, Y. S.; Gu, L.; Li, H.; Huang, X.; Chen, L. Three Dimensional Atomic Scale Observation of Structural Evolution of Cathode Material in a Working All Solid State Battery. *Nat. Commun.* **2018**, *9*, No. 3341.

(43) Tabata, H.; Ishii, E.; Okuda, H. Cation Antiphase Boundaries in Ionic Crystals Based on Anion Close Packing. *J. Cryst. Growth* **1981**, *52*, 956−962.

(44) Lee, S. Y.; Park, G. S.; Jung, C.; Ko, D. S.; Park, S. Y.; Kim, H. G.; Hong, S. H.; Zhu, Y.; Kim, M. Revisiting Primary Particles in Layered Lithium Transition Metal Oxides and Their Impact on Structural Degradation. *Adv. Sci.* **2019**, *6*, No. 1800843.

(45) Li, S.; Yao, Z.; Zheng, J.; Fu, M.; Cen, J.; Hwang, S.; Jin, H.; Orlov, A.; Gu, L.; Wang, S.; Chen, Z.; Su, D. Direct Observation of Defect Aided Structural Evolution in Ni Rich Layered Cathode. *Angew. Chem., Int. Ed.* **2020**, *59*, 22092−22099.

(46) Hong, L.; Yang, K.; Tang, M. A Mechanism of Defect Enhanced Phase Transformation Kinetics in Lithium Iron Phosphate Olivine. *npj Comput. Mater.* **2019**, *5*, No. 118.

(47) Wang, Z.; Guo, H.; Shao, S.; Saghayezhian, M.; Li, J.; Fittipaldi, R.; Vecchione, A.; Siwakoti, P.; Zhu, Y.; Zhang, J.; Plummer, E. W. Designing Antiphase Boundaries by Atomic Control of Hetero interfaces. *Proc. Natl. Acad. Sci. U.S.A.* **2018**, *115*, 9485−9490.

(48) Xu, X.; Liu, Y.; Wang, J.; Isheim, D.; Dravid, V. P.; Phatak, C.; Haile, S. M. Variability and Origins of Grain Boundary Electric Potential Detected by Electron Holography and Atom Probe Tomography. *Nat. Mater.* **2020**, *19*, 887−893.

(49) Gong, W.; Li, H.; Zhao, Z.; Chen, J. Ultrafine Particles of Fe, Co, and Ni Ferromagnetic Metals. *J. Appl. Phys.* **1991**, *69*, 5119−5121.

(50) Shibata, N.; Kohno, Y.; Nakamura, A.; Morishita, S.; Seki, T.; Kumamoto, A.; Sawada, H.; Matsumoto, T.; Findlay, S. D.; Ikuhara, Y. Atomic Resolution Electron Microscopy in a Magnetic Field Free Environment. *Nat. Commun.* **2019**, *10*, No. 2308.

(51) Lin, F.; Markus, I. M.; Doeff, M. M.; Xin, H. L. Chemical and Structural Stability of Lithium Ion Battery Electrode Materials under Electron Beam. *Sci. Rep.* **2014**, *4*, No. 5694.

(52) Wang, F.; Graetz, J.; Moreno, M. S.; Ma, C.; Wu, L.; Volkov, V.; Zhu, Y. Chemical Distribution and Bonding of Lithium in Intercalated Graphite: Identification with Optimized Electron Energy Loss Spectroscopy. *ACS Nano* **2011**, *5*, 1190−1197.

(53) Pokle, A.; Coelho, J.; Macguire, E.; Downing, C.; Casey, P.; Park, S. H.; McGuinness, C.; Nicolosi, V. EELS Probing of Lithium Based 2 D Battery Compounds Processed by Liquid Phase Exfoliation. *Nano Energy* **2016**, *30*, 18−26.

(54) Midgley, P. A.; Eggeman, A. S. Precession Electron Diffraction − a Topical Review. *IUCrJ* **2015**, *2*, 126−136.

(55) Viladot, D.; Véron, M.; Gemmi, M.; Peiró, F.; Portillo, J.; Estradé, S.; Mendoza, J.; Llorca Isern, N.; Nicolopoulos, S. Orientation and Phase Mapping in the Transmission Electron Microscope Using Precession Assisted Diffraction Spot Recognition: State of the Art Results. *J. Microsc.* **2013**, *252*, 23−34.

(56) Nam, K. W.; Yoon, W. S.; Yang, X. Q. Structural Changes and Thermal Stability of Charged LiNi$_{1/3}$Co$_{1/3}$Mn$_{1/3}$O$_2$ Cathode Material for Li Ion Batteries Studied by Time Resolved XRD. *J. Power Sources* **2009**, *189*, 515−518.

(57) Kim, A. Y.; Strauss, F.; Bartsch, T.; Teo, J. H.; Hatsukade, T.; Mazilkin, A.; Janek, J.; Hartmann, P.; Brezesinski, T. Stabilizing Effect of a Hybrid Surface Coating on a Ni Rich NCM Cathode Material in All Solid State Batteries. *Chem. Mater.* **2019**, *31*, 9664−9672.

(58) Momma, K.; Izumi, F. VESTA 3 for Three Dimensional Visualization of Crystal, Volumetric and Morphology Data. *J. Appl. Crystallogr.* **2011**, *44*, 1272−1276.

(59) Jones, L.; Yang, H.; Pennycook, T. J.; Marshall, M. S. J.; Aert, S. V.; Browning, N. D.; Castell, M. R.; Nellist, P. D. Smart Align—a New Tool for Robust Non Rigid Registration of Scanning Microscope Data. *Adv. Struct. Chem. Imaging* **2015**, *1*, 8.

(60) Lu, P.; Yan, P.; Romero, E.; Spoerke, E. D.; Zhang, J. G.; Wang, C. M. Observation of Electron Beam Induced Phase Evolution Mimicking the Effect of the Charge−Discharge Cycle in Li Rich Layered Cathode Materials Used for Li Ion Batteries. *Chem. Mater.* **2015**, *27*, 1375−1380.